aerospace

Article

Research on the Design and Bidirectional Work Process of Metal Diaphragms in Small Double-Pulse Solid Rocket Motors

Xueqin Du, Weihua Hui *, Youwen Tan, Wen Feng and Yang Liu

National Key Laboratory of Solid Rocket Propulsion, Northwestern Polytechnical University, Xi'an 710072, China;
duxueqin@mail.nwpu.edu.cn (X.D.); tanyouwen@mail.nwpu.edu.cn (Y.T.); fengwen@mail.nwpu.edu.cn (W.F.);
Liuy@nwpu.edu.cn (Y.L.)
* Correspondence: huiweihua@nwpu.edu.cn

Abstract: According to the requirements of the small double-pulse solid rocket motor, a compartmentalized isolation device has been designed. This device consists of a metal diaphragm and a support frame. An experimental study and numerical simulation were used to verify the bidirectional working process of the metal diaphragm during operation of the double-pulse motor. The results show that the pressure-bearing capacity of the metal diaphragm meets the requirements under the working conditions of pulse I without affecting pulse II, because the metal diaphragm can provide insulation and flame retardancy. The metal diaphragm can be cracked in the direction of the preset V-groove in a relatively short time under the working conditions of pulse II, which allows the gas to flow to the first pulse combustion chamber normally. This indicates that the metal diaphragm can meet the requirements of bidirectional working process in dual-pulse motors.

Keywords: double-pulse solid rocket motor; metal diaphragm; numerical simulation; pulse separation device

check for updates

Citation: Du, X.; Hui, W.; Tan, Y.; Feng, W.; Liu, Y. Research on the Design and Bidirectional Work Process of Metal Diaphragms in Small Double-Pulse Solid Rocket Motors. *Aerospace* **2024**, *11*, 848. https://doi.org/10.3390/aerospace11100848

Academic Editor: Jae Hyun Park

Received: 21 August 2024
Revised: 2 October 2024
Accepted: 10 October 2024
Published: 15 October 2024

1. Introduction

In recent years, human activities in space have increased. The successful development of various types of artificial satellites, space stations, probes, and other spacecraft is closely related to solid rocket motors [1,2]. A development trend of modern spacecraft is miniaturization. The use of small solid rocket motors can greatly reduce the mass occupied by the propulsion system, which offers advantages such as high mass ratio, high impulse-to-mass ratio, high safety, and low cost [3,4]. Small thrusters have great potential for future applications [5]. Small double-pulse solid rocket motors utilize pulse separation devices (PSDs) for interstage isolation of the combustion chambers. PSDs divide the combustion chamber into two distinct chambers, each with an independent ignition device. By adjusting the thrust distribution and the interval between the two-stage pulses, the spacecraft's flight trajectory can be better controlled and the motor energy better managed [6–8]. Additionally, double-pulse motors can be used to fly mission-adapted trajectories [9].

PSDs are one of the core components of double-pulse motors. PSDs can be categorized as hard PSDs or soft PSDs [4,10–14]. Among hard PSDs, there are two main structural types: ceramic configuration [15] and metal piece configuration [16–19]. The metal diaphragms, which are metal-piece-type PSDs, play the role of being pressure-bearing and flame-retardant [7]. It consists of a metal diaphragm and a supporting frame [20]. The metal diaphragm is closely affixed to the support frame. To reliably control the opening pressure and the size of the rupture, a certain number of grooves can be set up on the side of the rupture facing the direction of the first pulse.

The two-way working process of the metal diaphragm in the double-pulse motor includes withstanding gas pressure during operation of the first pulse and opening quickly at a certain pressure during operation of the second pulse. The diaphragm needs to remain intact and sealed during the first pulse and then be able to open quickly and reliably to allow the second pulse to be initiated. Therefore, the metal diaphragm needs to meet the following requirements: (1) During the operation of the first-pulse motor, the metal diaphragm can withstand the gas pressure and insulate the flame retardant, to prevent the second-pulse combustion chamber from being affected; (2) during operation of the second-pulse motor, the metal diaphragm can be opened quickly at a suitable pressure to ensure the gas flows into the first-pulse combustion chamber as required.

Since the development of a double-pulse solid rocket motor based on the fragile diaphragm design concept by Bayer-Chemie/Protac (Aschau am Inn, Germany) in 1994 [16], many researchers have conducted numerical simulations and experiments on metal diaphragms. Liu WK et al. [17] investigated the opening characteristics of metal diaphragms. The researchers employed the ductile-damage model and Brittle cracking model to simulate the static and dynamic opening processes of the diaphragm and conducted corresponding cold-flow static opening and hot-flow dynamic opening experiments. It is concluded that the static opening pressure of the diaphragm is obviously higher than the dynamic opening pressure. Zhou XX et al. [18] analyzed the influence of metal diaphragm materials and structural parameters on the opening performance using explicit dynamic simulations and experiments. Their results showed that the copper diaphragm had a breakout angle about 1.7 times higher than the aluminum diaphragm, which could better prevent debris ejection during diaphragm opening. They also found that the depth of the pre-positioning groove was inversely related to the opening pressure of the metal diaphragm, with a deeper groove resulting in a lower opening pressure. Xuan W et al. [19] employed a modified Johnson–Cook principal structural model and damage criterion to simulate the pressure-bearing capacity of the diaphragm structure. The results showed that when the preset slot depth was large, the depth was the main factor affecting the diaphragm opening pressure, whereas when the slot depth was small, the slot width had a more obvious effect on the diaphragm opening pressure. Li et al. [21] conducted numerical simulations on metal diaphragms. The simulation results showed that the diaphragms could meet the requirements of I-pulse pressure under the supporting frame’s action. Furthermore, through four simulations with different pressure build-up times, the results revealed that the pressure build-up speed was negatively correlated with the opening pressure.

Previous studies have primarily focused on the state and characteristics of metal diaphragms at specific working stages. For instance, they have investigated the opening pressure of metal diaphragms and its influencing factors during the second-pulse operation through simulations and experiments. However, these studies lacked a comprehensive analysis of the complete working process of metal diaphragms in double-pulse motors. Alternatively, the working characteristics of metal diaphragms in double-pulse motors have only been studied through simulations, without experimental verification.

In this study, a double-pulse motor and a pulse separation device meeting the requirements of bidirectional operation were designed and fabricated. Three groups of characteristic experiments were effectively conducted to verify the performance. Combined with simulation analysis and comparison, a simulation method for the bidirectional operation analysis of the metal diaphragm was established. This allowed the complete bidirectional operation of the double-pulse motor to be realized.

2. Structural Design of the Small Double-Pulse Motor and Separation Device

The designed small double-pulse motor, as shown in Figure 1, consists of several key components including combustion chambers, a nozzle, an ignition device, and a separation device. The blue box in Figure 1 indicates the location of the separation device, which comprises support frames and a metal diaphragm. The design of the separation device is primarily based on the research by Shi Rui et al. [22]. The main support is provided by the cross-type support frame near the second-pulse motor, while the support frame near the first-pulse motor primarily serves a fixation role. For the subsequent analysis, the cross-type support frame and the diaphragm are considered the key components of the pulse separation device.

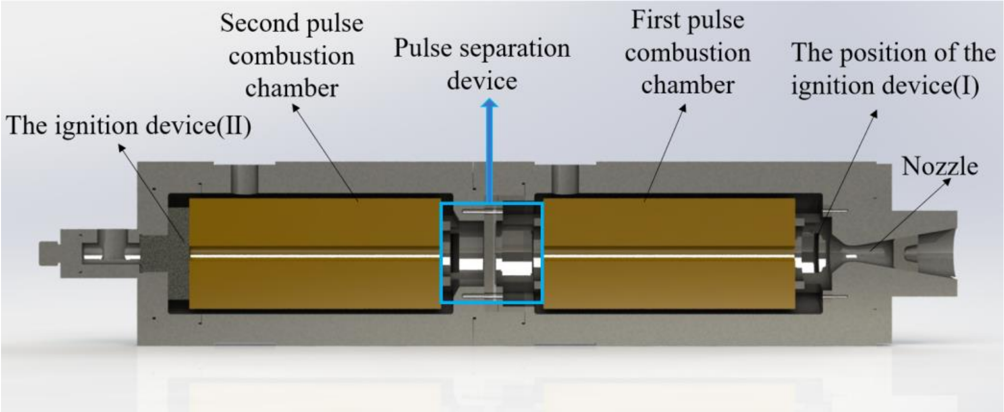

Figure 1. The longitudinal section of the double-pulse motor.

The structure of the cross-type support frame and the metal diaphragm is depicted in Figure 2. The metal diaphragm features a V-groove design on one side, with four grooves of 0.5 mm depth and 1 mm width, as shown in Figure 2b,c. The grooved side of the diaphragm faces the first-pulse combustion chamber, while the smooth side faces the second-pulse combustion chamber. The metal diaphragm and support frame are tightly connected via screws. The material for the metal diaphragm is 1060#Al, and the support frame is fabricated from 45# steel. The material properties are provided in Table 1. The propellant used in the motor is a tube-type column charge composed of cobalt-2. The double-pulse motor and charge configuration are consistent across the subsequent tests.

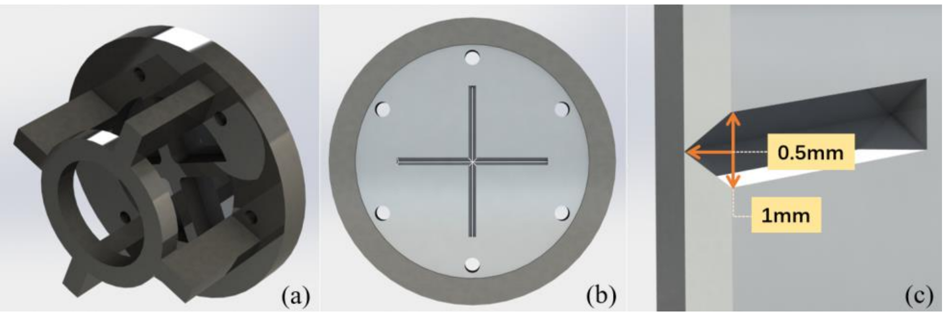

Figure 2. (**a**) The structure of the cross-support frame; (**b**) the metal diaphragm plate (pulse I view); (**c**) the dimensions of the V-grooves.

Table 1. Material parameters [23–25].

	Density (g/cm^3)	Young's Modulus (GPa)	Poisson's Ratio	Tensile Strength (MPa)	Yield Strength (MPa)
1060# Al	2.68	70	0.33	150	66
45# steel	7.85	216	0.3	800	355

3. Verification of the Pressure-Bearing Capacity

3.1. Simulation Analysis on the Pressure-Bearing Capacity of the PSD

3.1.1. Finite Element Model under I Pulse Working Condition

Abaqus static simulation was utilized to model the pressure-bearing behavior of the separation device. The full separation device assembly was selected as the computational model. The simulation accounted for the supporting effect of the support frame on the diaphragm during operation. As shown in Figure 1, the metal diaphragm and support frame are fixed to the engine housing via threaded connections. Figure 2 illustrates that there are six threaded connections on the separation device, which appear relatively stable.

To simplify the analysis, the threaded connections are assumed to have negligible influence on the structural behavior. The contact between the metal diaphragm and the support frame is the tie constraint. The mesh element employed for the entire assembly is C3D10. The C3D10 mesh element is a suitable choice for Abaqus static analyses as it provides a balanced approach between modeling fidelity, computational efficiency, and numerical robustness. Detailed information on the mesh used for the separation device is provided in Table 2.

Table 2. Information on the mesh used for the metal diaphragm and support frame.

	Number of Nodes	**Number of Elements**	**Approximate Global Size**
The metal diaphragm	47,833	28,032	0.6 mm
The support frame	28,257	16,828	1.3 mm

The finite element mesh of the support frame and metal diaphragm is shown in Figure 3a. In order to realistically and reliably simulate the state of the metal diaphragm during operation of the first-pulse motor, the support frame boundary condition was set to be completely fixed, and the application area was the red area in Figure 3b. The pressure was applied to the side of the metal diaphragm facing the pulse I combustion chamber, which is shown in the red area in Figure 3c. This pressure value was 11 MPa, which was slightly greater than the maximum operating pressure predicted for the first pulse. The duration of applying pressure was 0.9 s, which was approximate to the predicted working time of the first pulse.

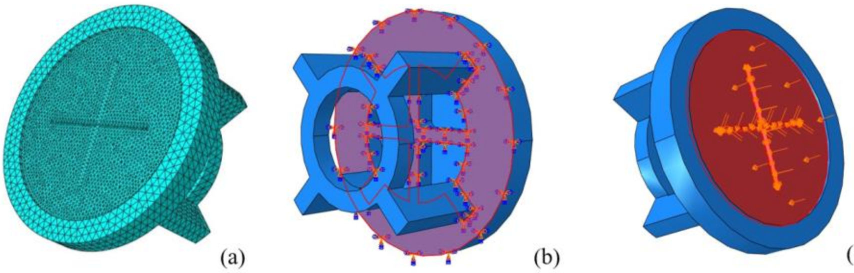

Figure 3. (**a**) The mesh model; (**b**) the boundary condition; (**c**) the working load of the PSD.

3.1.2. Simulation Results and Analysis on the Pressure Bearing Capacity of the PSD

The stress distribution obtained from the simulation is shown in Figures 4 and 5. Under a compressive load of 11 MPa, the maximum stress in the metal diaphragm was 139 MPa. This peak stress was primarily located at the root of the load application region and the depression. The maximum stress in the support frame was 377 MPa. This occurred at the cross and circumferential edges. However, the stresses applied to both the metal diaphragm and the support frame were within their respective tensile strengths. The presence of the support frame significantly enhanced the pressure-bearing capacity of the metal diaphragm. This enabled the diaphragm to maintain a safe and reliable sealing effect under the larger operating pressure of pulse I. Furthermore, it ensured the diaphragm will not be adversely affected by the combustion chamber conditions during pulse II.

3.2. Experimental Study on Pressure-Bearing Capacity of the PSD

3.2.1. Experimental Setup under I Pulse Working Condition

The test setup utilized a double-pulse motor, as depicted in Figure 1. Pressure sensors were installed in both the pulse I and pulse II combustion chambers. Since the verification focused on the pressure-bearing capacity of the metal diaphragm, a solid propellant charge was loaded into the pulse I combustion chamber. The ignition device and ignition powder (black powder) were used for the ignition tool.

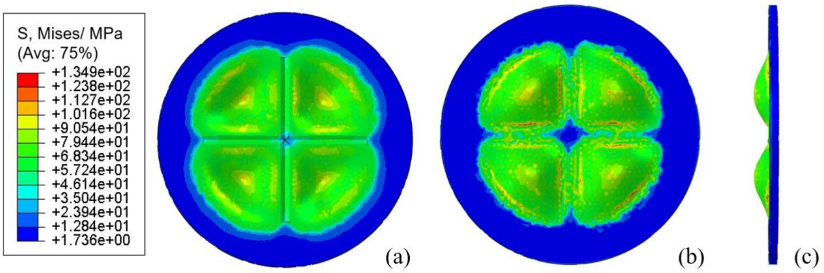

Figure 4. Von Mises stress contour plot of the metal diaphragm: (**a**) pulse I view; (**b**) pulse II view; (**c**) lateral view.

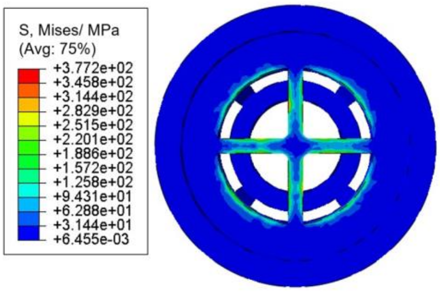

Figure 5. Von Mises stress contour plot of the support frame.

3.2.2. Experimental Results and Analyses on Pressure-Bearing Capacity of the PSD

The metal diaphragm and the support frame after the experiment are shown in Figure 6. From the perspective of the pulse I combustion chamber, the condition of the metal diaphragm had been observed. This observation indicated that the metal diaphragm did not rupture during operation of the pulse I motor. The metal diaphragm had been found to be deformed to a certain extent, as depicted in Figure 7. The side of the diaphragm in contact with the support frame had clearly exhibited the shape of the cross. However, the overall metal diaphragm had remained unbroken. The experiment results aligned with the simulation findings. This suggested that the metal diaphragm can withstand the gas pressure, heat, and flame-retardant conditions during operation of the pulse I motor. As a result, the pulse II combustion chamber was not affected.

The pulse I motor was successfully ignited and operated normally. After the propellant was burned, the shell remained intact. Figure 8 depicts the pressure change curves for both the pulse I and pulse II motors during the operational process. The pressure of the pulse I motor rapidly increased, reaching a maximum of approximately 10 MPa. After operating for around 0.8 s, the pressure then decreased, indicating the completion of the pulse I motor's work. Importantly, throughout this entire process, the pressure of the pulse II motor remained essentially unchanged. This observation suggests that the metal diaphragm did not rupture.

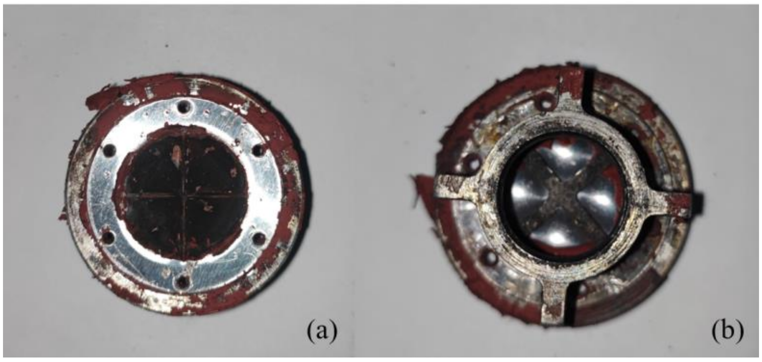

Figure 6. (**a**) The metal diaphragm; (**b**) the cross-type support frame after the experiment.

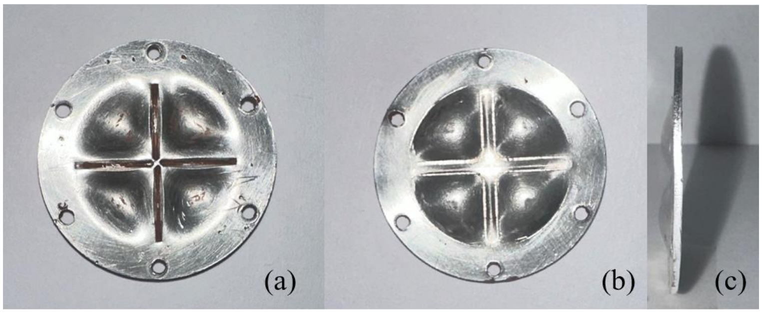

Figure 7. Metal diaphragm after the experiment: (**a**) pulse I view; (**b**) pulse II view; (**c**) lateral view.

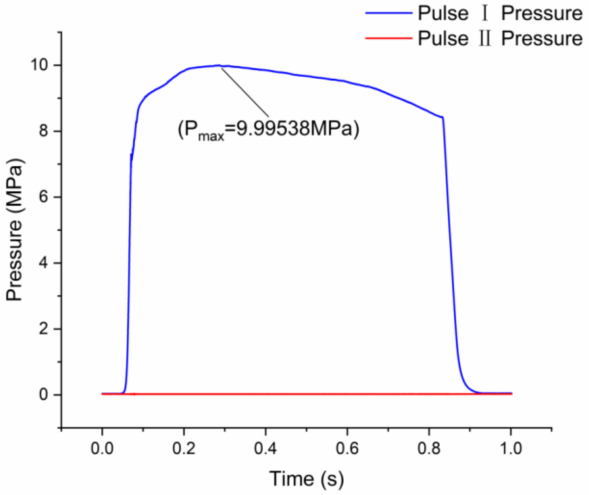

Figure 8. Pressure profile during the operation of the pulse I motor.

4. Verification of the Opening Pressure

4.1. Simulation Analysis on the Opening Pressure of the Diaphragm

4.1.1. Theoretical Model of Explicit Dynamics and Ductile Damage

The process of the diaphragm opening was calculated using an explicit-dynamics theory coupled with the finite-element method. This approach simplifies the solution process. Traditional finite-element methods require recalculating the stiffness matrix at each time step. They also need repeated iteration. This consumes substantial time and storage. In contrast, the explicit-dynamics–finite-element method can omit these two steps. It uses the central-difference method to solve finite-element equations explicitly. This can improve computational speed and reduce storage requirements. It also maintains good computational stability.

The basic equation for the explicit-dynamics approach is as follows:

$$M\ddot{a}_t + C\dot{a}_t + Ka_t = Q_t$$

where M is the mass matrix, C is the damping matrix, K is the stiffness matrix, $\ddot{a}_t$ is the acceleration vector, $\dot{a}_t$ is the velocity vector, a_t is the displacement vector, and Q_t is the force vector. This explicit formulation allows the acceleration vector $\ddot{a}_t$ to be calculated directly from the other terms, without the need to invert the mass matrix or iterate to solve for the displacements. This explicit solution approach is computationally efficient and avoids the challenges associated with the implicit formulation used in traditional finite-element methods.

In the explicit-dynamics–finite-element method, the central-difference scheme is primarily used to perform explicit integration of the equations of motion. The central-difference formula approximates the velocity and acceleration terms as follows:

$$\dot{a}_t = (-a_{t-\Delta t} + a_{t+\Delta t})/(2\Delta t)$$

$$\ddot{a}_t = (a_{t-\Delta t} - 2a_t + a_{t+\Delta t})/\Delta t^2$$

where Δt is the time step.

Substituting these expressions into the basic equation of motion, can derive the recursive-update formula:

$$\left(\frac{1}{\Delta t^2}M + \frac{1}{2\Delta t}C\right)a_{t+\Delta t} = Q_t - \left(K - \frac{2}{\Delta t^2}M\right)a_t - \left(\frac{1}{\Delta t^2}M - \frac{1}{2\Delta t}C\right)a_{t-\Delta t}$$

The failure process of metal diaphragms is primarily a failure behavior of the material under internal pressure load. The uniaxial tensile stress–strain curve of a typical metal specimen is shown in Figure 9. The OA section represents the linear elastic deformation stage. The AB section represents the plastic yield stage. After exceeding point B, the load-bearing capacity of the material decreases significantly. The material fails when it reaches point C. By incorporating the plastic model, the ductile-damage model can simulate the damage characteristics of materials after entering the plastic stage. If the damage of the material is not considered, the strength of the material will increase slowly in the plastic stage. However, after considering the damage effect, the material strength of the damaged part will be reduced. The overall material strength will show a downward trend until it is completely destroyed.

In the finite-element analysis, a damage evolution approach was employed to model the failure behavior of the materials. Specifically, the damage initiation was defined based on the equivalent plastic strain at the onset of damage, referred to as the fracture strain. This fracture strain parameter was used as the damage initiation criterion in the simulation. Furthermore, the displacement at failure was specified in the damage evolution law. This parameter represents the displacement value from the initiation of damage to the complete failure and fracture of the material. According to the stress–strain characteristics of 1060 aluminum reported in the literature [26], the following damage parameters were adopted in the present study: 0.015 for fracture strain and 0.2 for displacement at failure. This damage modeling approach allowed accurate representation of the complete damage and failure process of the 1060 aluminum material within the finite-element framework, supporting reliable prediction of the rupture behavior of the diaphragm.

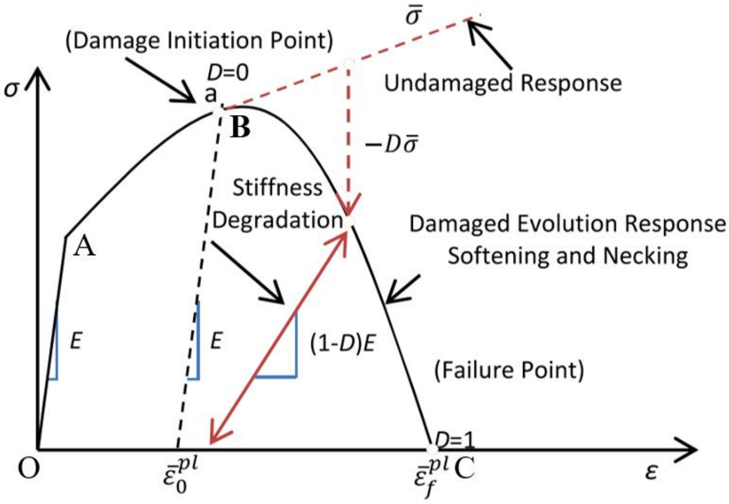

Figure 9. The uniaxial tensile stress–strain curve of a typical metal specimen [27].

4.1.2. Finite-Element Model under II Pulse Working Condition

Simulation was performed using Abaqus explicit dynamics, and the diaphragm was selected as the computational model. The pulse II combustion chamber is located on one side of the support frame. During the operation of the pulse II motor, the support frame does not provide any structural support to the metal diaphragm. Once gas is generated, the metal diaphragm becomes deformed and no longer maintains contact with the support frame. Therefore, the influence of the support frame on the metal diaphragm can be neglected. The mesh element employed for the diaphragm was C3D10M. The C3D10M element is often preferred for modeling the nonlinear behavior of solid structures. It is suitable for simulating the failure process of metal diaphragms under internal pressure loading, as it can better capture the complex material response. The detailed mesh information for the metal diaphragm is provided in Table 3.

Table 3. Information on the mesh of the metal diaphragm.

	Number of Nodes	Number of Elements	Approximate Global Size
The metal diaphragm	69,658	41,439	0.5 mm

The finite-element mesh of the metal diaphragm is shown in Figure 10a. In order to realistically and reliably simulate the state of the metal diaphragm during operation of the second-pulse motor, the diaphragm boundary condition is set to be completely fixed, and the application area is the red area in Figure 10b. The pressure is applied to the side of the metal diaphragm facing the pulse II combustion chamber, which is shown in the red area in Figure 10c. A linearly increasing load is applied to the side of the metal diaphragm facing the pulse II combustion chamber. This is performed to simulate the process of the diaphragm being broken by the gas generated during the pulse ignition. The applied load is such that the pressure increases linearly from 0 MPa to 5 MPa over a duration of 3 ms. The corresponding opening pressure can be determined based on the time at which the metal diaphragm opens.

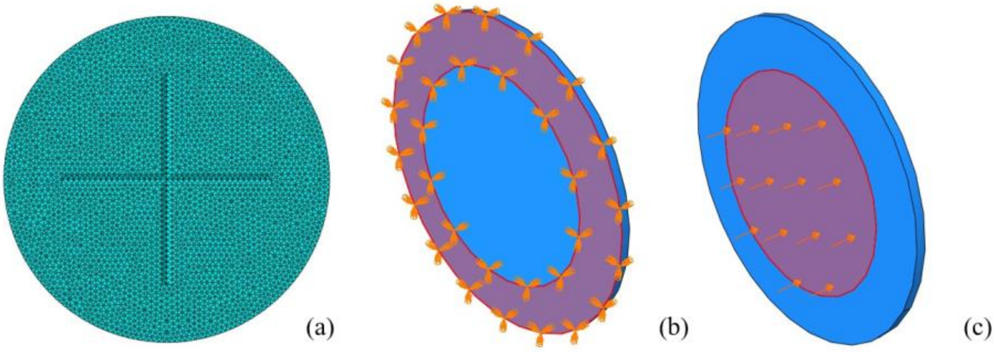

Figure 10. (**a**) The mesh model; (**b**) the boundary condition; (**c**) the working load of the diaphragm.

4.1.3. Simulation Results and Analysis of the Opening Pressure

The stress distribution of the metal diaphragm during pressure loading is depicted in Figure 11. At t = 1.92 ms, the center of the metal diaphragm exhibits an initial fracture. Subsequently, the fracture propagates along the V-groove. The crack range expands progressively. By t = 2.0588 ms, the entire V-groove has completely cracked. The total duration of this cracking process is approximately 0.1388 ms. The average time at which the metal diaphragm is considered to have fully opened is t = 1.989 ms. Based on the applied linear load, the opening pressure of the metal diaphragm is determined to be 3.3 MPa.

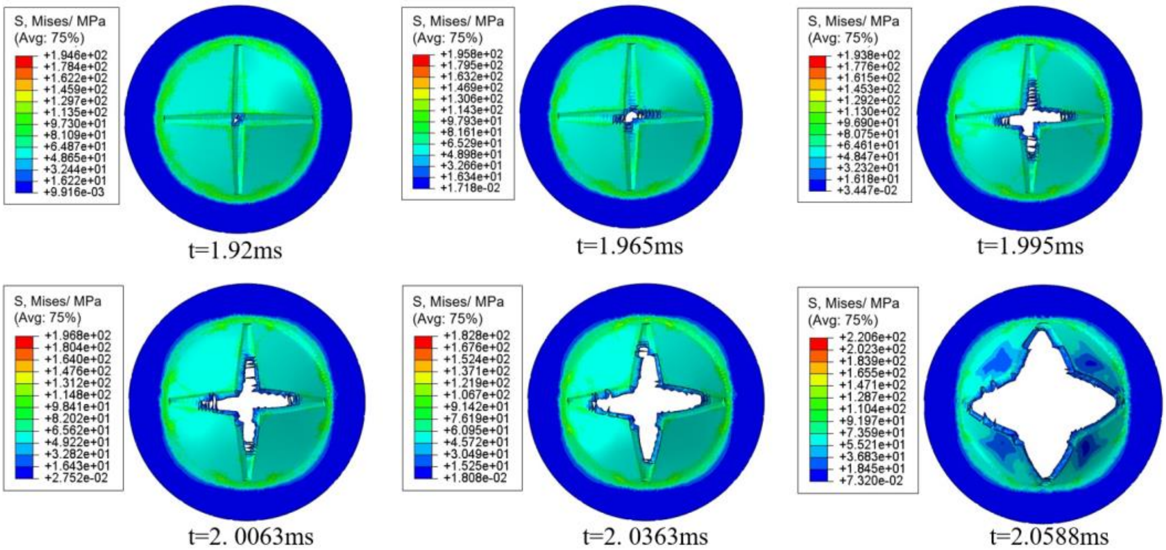

Figure 11. Von Mises stress contour plot of the metal diaphragm at six moments.

4.2. Experimental Study on the Opening Pressure

4.2.1. Experimental Setup under II Pulse Working Condition

The test device employs a double-pulse motor, as shown in Figure 1. Pressure sensors are installed in both the pulse I and II combustion chambers. The focus of this study is on the opening pressure of the diaphragm after the ignition of the pulse II motor. To this end, only ignition powder, specifically black powder, is installed in the pulse II combustion chamber, without any propellant.

4.2.2. Experimental Results and Analyses of the Opening Pressure

After the test, the motor was disassembled. The structures are shown in Figure 12. Inspection revealed no damage to the motor case. However, the ignition tool exhibited ablation. The overall structure remained intact. The metal diaphragm was cracked into four flaps along the V-groove, but the root was not broken. The metal diaphragm was removed from the separation device. Its deformation is depicted in Figure 13. As shown in Figure 13a,b, the metal diaphragm cracked along the V-groove. This is consistent with the simulation results presented in Figure 11. The absence of debris production indicates that the metal diaphragm broke open during operation of the pulse II motor. The pre-designed V-groove allowed the diaphragm to break in a controlled manner, generating less debris. Figure 13c,d provide a comparison between the test and simulation results for the side of the metal diaphragm. The maximum deformation of the metal diaphragm after the test was measured to be 8.3 mm. The simulation calculated a deformation of 8.19 mm, resulting in an error of 1.32%.

Figure 14 depicts the variation in pressure in the pulse I and pulse II chambers over time. The data show that the pulse II pressure reaches a peak value of 3.11 MPa at t = 0.018 s, after which it begins to decrease. Notably, the pulse I pressure starts to rise almost simultaneously with the pulse II pressure reaching its peak. At t = 0.024 s, the pressures in the I and pulse II chambers equalize at 1.91822 MPa, and they remain synchronized thereafter. The subsequent pressure decrease can be attributed to the small amount of ignition charge used. From the pressure curve, the opening pressure of the metal diaphragm can be determined as 3.11 MPa. This value is in close agreement with the simulation result of 3.3 MPa, with an error of only 5.7%. After the metal diaphragm is opened, the gas in the pulse II chamber flows into the pulse I chamber, resulting in a pressure balancing process between the two combustion chambers.

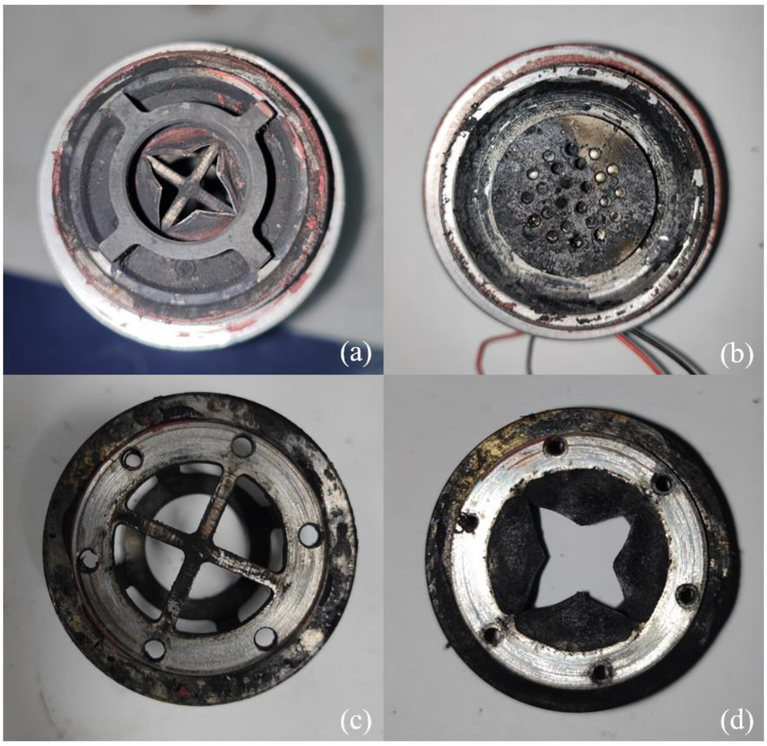

Figure 12. Components of the motor after the experiment: (**a**) pulse II combustion chamber and separation device; (**b**) ignition apparatus; (**c**) support frame; (**d**) metal diaphragm.

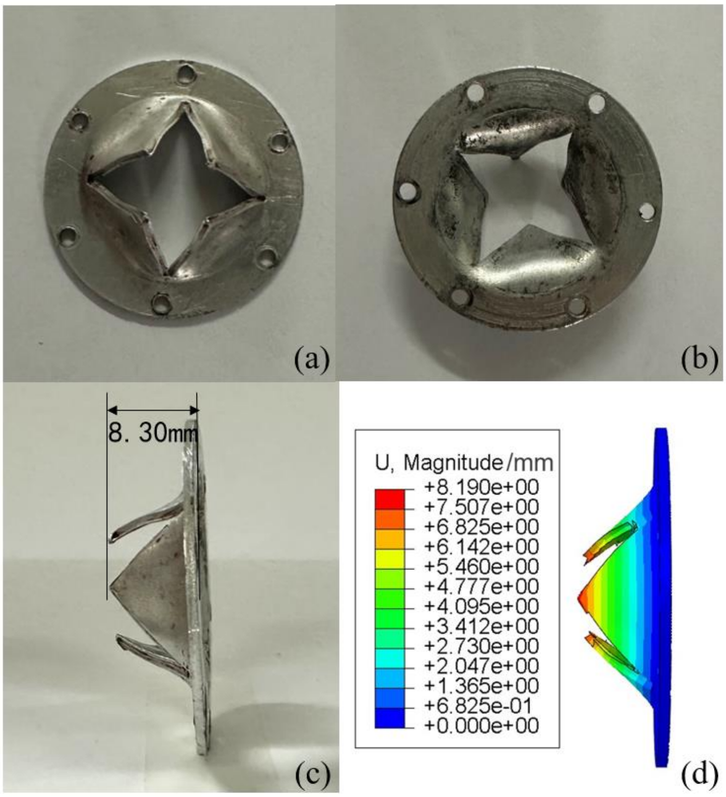

Figure 13. Metal diaphragm after the experiment: (**a**) slotted side; (**b**) smooth side; (**c**) lateral side; (**d**) deformation of the metal diaphragm.

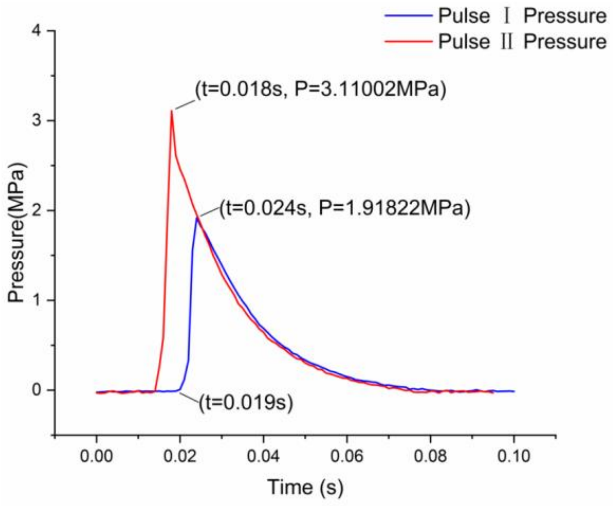

Figure 14. Pressure profile of pulse I and pulse II in the test.

5. Double-Pulse Motor Experiment

The experimental setup utilized a double-pulse motor, as depicted in Figure 1. Both combustion chambers were filled with propellant. Ignition tools were installed at both ends of the motor, and pressure sensors were positioned in each combustion chamber. The assembled motor is shown in Figure 15.

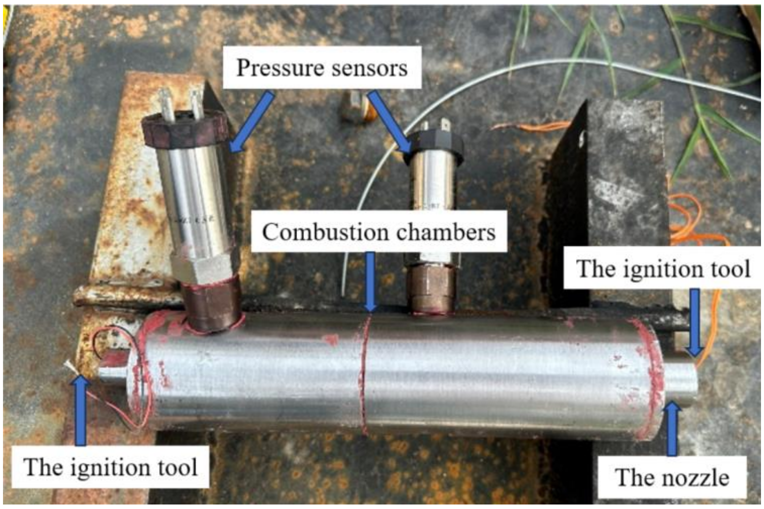

Figure 15. Double-pulse motor before the experiment.

The pulse I ignition device was connected to the power supply at t = 0.0 s. After a 0.01 s delay, smoke and a flame were observed emanating from the nozzle. The smoke then dissipated, and the flame stabilized. At t = 0.8 s, the flame reached its most prominent state. Subsequently, at t = 0.82 s, the flame disappeared, and white smoke appeared. This white smoke persisted for a period of time before eventually dissipating. The complete sequence of events is depicted in Figure 16.

The power to the pulse II ignition device was then activated, with this event designated as the t = 0.0 s reference point. After a 0.03 s delay, a substantial volume of white smoke was observed emanating from the nozzle. This was followed by a flame spray within the nozzle. At t = 0.84 s, the flame disappeared, and a continuous white smoke discharge was noted from the nozzle. The complete sequence of events is depicted in Figure 17.

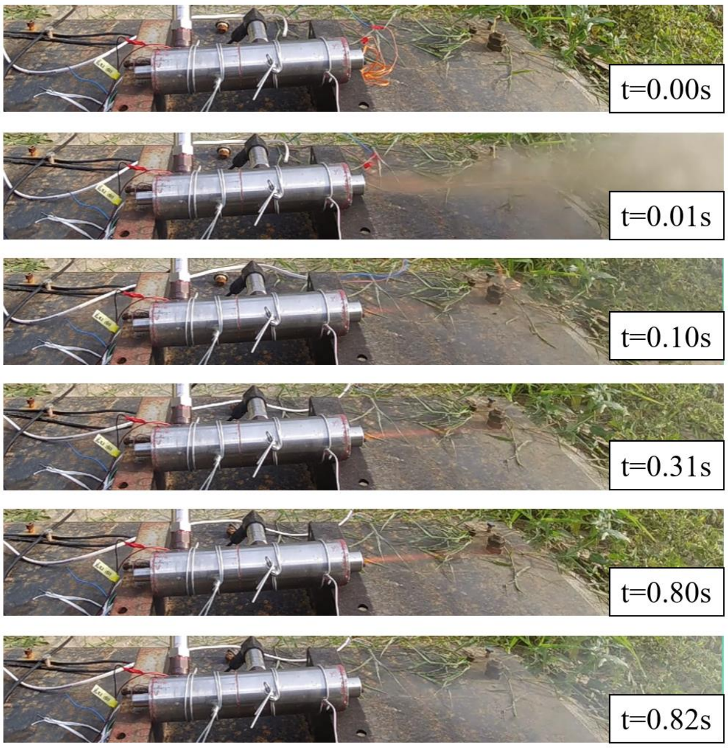

Figure 16. Working process of the pulse I motor.

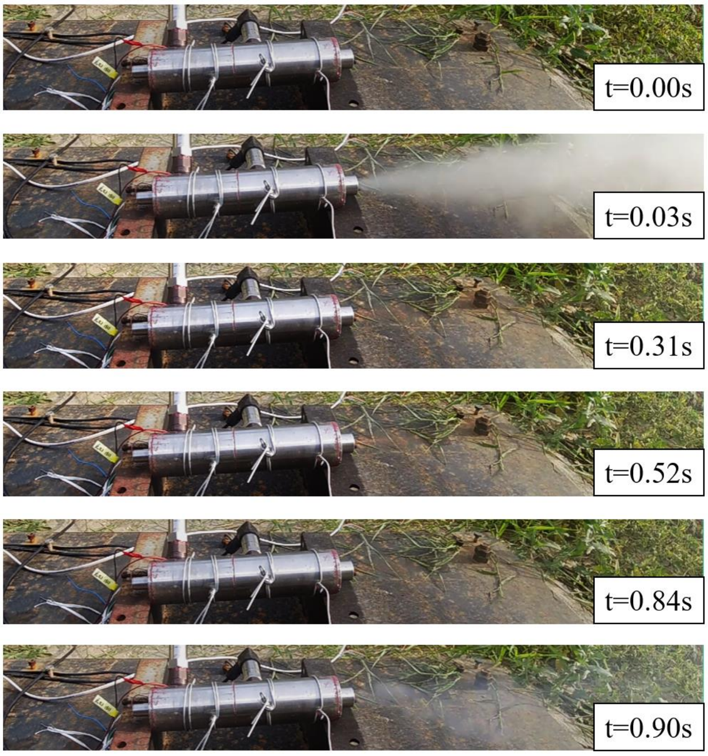

Figure 17. Working process of the pulse II motor.

A post-test inspection of the motor revealed no damage to the motor casing. However, ablation of the support bracket was observed. Additionally, the metal diaphragm was found to be broken open, with no remnants of the diaphragm remaining within the motor. The metal diaphragm was subsequently removed and examined, revealing that it had fractured at the root, as depicted in Figure 18.

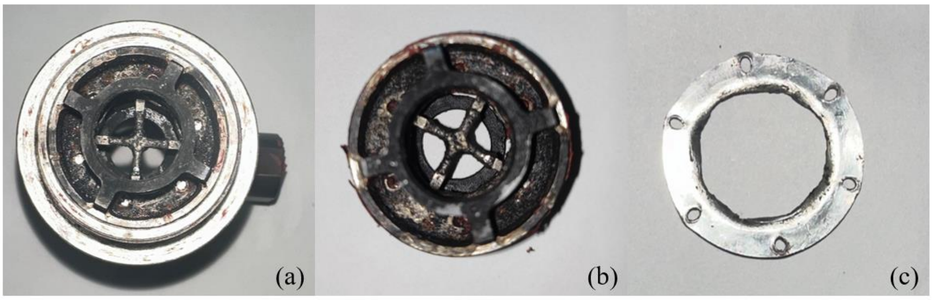

Figure 18. Components of the motor after the experiment: (**a**) the pulse II motor section; (**b**) the support frame; (**c**) the metal diaphragm.

Pressure sensors were installed at the front and rear of the motor. Figure 19 shows the variation curves of the two combustion chamber pressures during operation of the pulse I motor. The interval time between the pressure rising to 10% of the maximum after motor ignition and falling to 10% of the maximum is defined as the motor's working time [28]. The working time of the pulse I motor is about 0.8 s, which matches the working process shown in Figure 16. From the pulse II pressure curve, it can be seen that the pressure remained unchanged from the initial value during the entire working time of pulse I. This indicates the metal diaphragm could withstand the gas pressure and insulate the flame, so the pulse II combustion chamber was not affected.

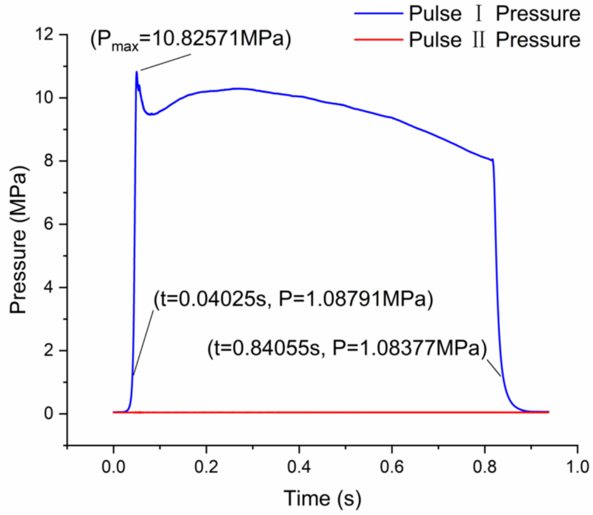

Figure 19. Pressure profile of the pulse I motor during operation.

Figure 20 depicts the variation curves of the two combustion chamber pressures during operation of the pulse II motor. The inset shows an enlarged view of the green boxed region. At t = 0.0305 s, the pulse II pressure peaked at 4.13363 MPa. Concurrently, at t = 0.3055 s, the pulse I pressure began to rise as the pulse II pressure decreased. The pressures in the two chambers then equalized. Based on the motor structure, it is believed that when the pulse II chamber pressure reached 4.13 MPa, the metal diaphragm opened. This allowed gas to flow from the pulse II chamber to the pulse I chamber. The synchronization of the chamber pressures suggests the gas outflow speed from the pulse II chamber was lower than the pressure build-up rate. As the propellant fully ignited, the pressure then rose rapidly. The analysis indicates the metal diaphragm can open rapidly during pulse II ignition to enable normal operation of the motor. The opening pressure was 4.13 MPa, occurring 3.1 ms after ignition. In the pulse II verification test, the measured opening pressure was 3.11 MPa. This was potentially due to partial propellant ignition leading to premature diaphragm breakage, after which the pressure continued to rise briefly.

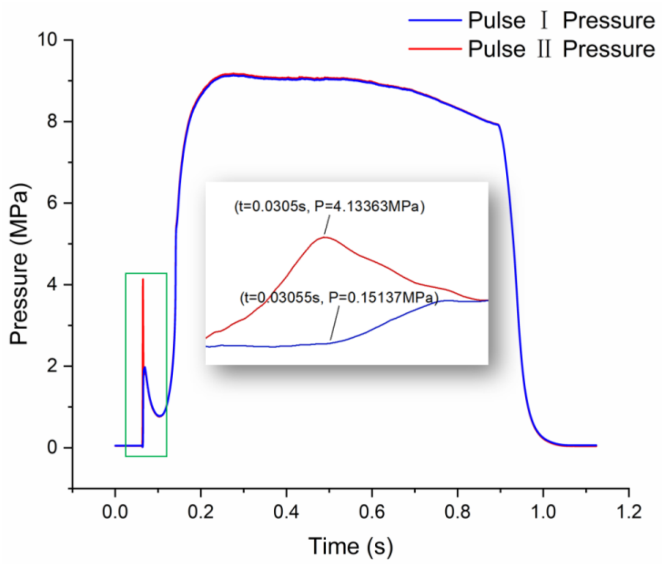

Figure 20. Pressure profile of the pulse II motor during operation.

6. Conclusions

The bidirectional working process of a double-pulse SRM is investigated in this paper, and the conclusions are as follows:

(1) The metal diaphragm can withstand high-pressure gas. It is also heat-insulated and flame-retardant when the pulse I motor is operating. Furthermore, the support frame enhances the pressure-bearing capacity of the metal diaphragm. Abaqus static simulation applying 11 MPa pressure for 0.9 s showed that the maximum stress value was less than the pressure limit. The finite-element simulation can provide a reliable reference for designing the pressure-bearing capacity of the metal diaphragm;

(2) The measured opening pressure during the pulse II test of the metal diaphragm was 3.11 MPa. The opening pressure obtained through the ductile-damage model and Abaqus explicit-dynamics simulation was 3.3 MPa, with an error of 5.7%. This simulation result can serve as a reference for the design of the metal diaphragm. The opening pressure obtained in the double-pulse test is 25% higher than the simulation and pulse II, likely due to the effect of charge burning on the pressure build-up rate;

(3) The designed separation device has been verified to meet the bidirectional working requirements through the double-pulse motor test, ensuring the normal operation of the motor. These findings provide a solid foundation for the further development and optimization of the pulse separation device.

Author Contributions: Methodology, X.D., W.H. and Y.L.; Software, X.D., Y.T. and W.F.; Formal analysis, Y.T. and Y.L.; Resources, W.H. and Y.L.; Data curation, Y.T.; Writing—original draft, X.D.; Visualization, W.F. All authors have read and agreed to the published version of the manuscript.

Funding: This article was funded by the Fundamental Research Funds for the Central Universities (No. D5000230316).

Data Availability Statement: The original contributions presented in the study are included in the article, further inquiries can be directed to the corresponding author.

Conflicts of Interest: The authors declare no conflict of interest.

References

1. Okninski, A. Solid rocket propulsion technology for de-orbiting spacecraft. *Chin. J. Aeronaut.* **2022**, *35*, 128–154. [CrossRef]
2. Jarry, A.; Bonnal, C.; Dupont, C.; Missonnier, S.; Lequette, L.; Masson, F. SRM plume: A candidate as space debris braking system for Just-in-Time Collision avoidance maneuver. *Acta Astronaut.* **2019**, *158*, 185–197. [CrossRef]
3. Xu, J.; Zhang, J.; Li, F.; Liu, S.; Ye, Y.; Shen, R. A review on solid propellant micro-thruster array based on MEMS technology. *FirePhysChem* **2023**, *4*, 95–106. [CrossRef]

4. Zhang, K.; Wang, C.; Tian, W. Study on the ablation mechanism of the first pulse insulation layer in a double-pulse solid rocket motor. *Aerospace* **2022**, *9*, 590. [CrossRef]
5. Koehler, F.; Meisner, M.; Vollin, J. Multi-pulse solid rocket motor technology. In Proceedings of the AIAA Propulsion and Energy 2020 Forum, Virtual, 24–28 August 2020; pp. 1–6.
6. Wang, C.; Liu, H.; Yang, D. Research on the Development of Separation Device in Pulse Solid Rocket Motor. *Aero Weapon.* **2012**, *26*, 48–51.
7. Wang, C.G.; Liu, H.C.; Yang, D.M.; Chen, C. Study of development status and future development proposals for pulse soild rocket motor. *Appl. Mech. Mater.* **2012**, *110*, 2354–2358. [CrossRef]
8. Guan, S.; Hu, F. Research on multiple pulse solid rocket motor technology with port cover. *Tactial Missile Technol.* **2015**, *4*, 59–65.
9. Naumann, K.W.; Stadler, L. Double-pulse solid rocket motor technology—Applications and technical solutions. In Proceedings of the 46th AIAA/ASME/SAE/ASEE Joint Propulsion Conference and Exhibit, Nashville, TN, USA, 25–28 July 2010.
10. Liu, W.; Chen, X.; Li, Y. Numerical simulation on cold-flow impact of the soft pulse separation device in dual pulse solid rocket motor. *J. Phys. Conf. Ser.* **2020**, *1510*, 012016. [CrossRef]
11. Zhang, J.; Li, Y.; Han, F.; Yan, D. Characteristics of plug motion in dual pulse solid rocket motor. *J. Aerosp. Power* **2021**, *36*, 216–224.
12. Dian, Y.L.; Li, Y.; Xu, J.; Li, H.; Wu, G. Study on Large Deformation Characteristics of Soft Interlayer in Pulsed Solid Rocket Motor. *J. Ballist.* **2023**, *35*, 1–7.
13. Stadler, L.; Hoffmann, S.; Huber, J.; Naumann, K.; Stingl, R. The flight demonstration of the double pulse motor demonstrator MSA. In Proceedings of the 46th AIAA/ASME/SAE/ASEE Joint Propulsion Conference and Exhibit, Nashville, TN, USA, 25–28 July 2010.
14. Stadler, L.; Hoffmann, S.; Niedermaier, H.; Hacker, A.; Bénayon, G.; Trouillot, P.; Naumann, K. Testing and verification of the LFK NG dual pulse motor. In Proceedings of the AIAA/ASME/SAE/ASEE 42nd Joint Propulsion Conference, Sacramento, CA, USA, 9–12 July 2006; pp. 4426–4439.
15. Wang, C.H.; Liu, Y.; Liu, Y.B. Design and experimental studies on ceramic port cover for dual pulse motor. *Acta Astronaut.* **2011**, *68*, 1881–1890. [CrossRef]
16. Naumann, K.; Stadler, L.; Trouillot, P.; Weigand, A.; Zanelli, D.; Schilling, S. Double-pulse solid rocket technology at Bayern-Chemie/Protac. In Proceedings of the 42nd AIAA/ASME/SAE/ASEE Joint Propulsion Conference and Exhibit, Sacramento, CA, USA, 9–12 July 2006.
17. Liu, W.K.; He, G.Q.; Wang, C.G. Research on Dynamic and Static Opening of Metal Diaphragm in Double Pulse Solid Rocket Motor. *J. Propuls. Technol.* **2014**, *35*, 1259–1264.
18. Zhou, X.X.; Meng, H.L.; Luo, Y.Z. Research on the opening performance of metal diaphragm in compartment double-pulse SRM. *J. Solid Rocket. Technol.* **2022**, *45*, 332–336.
19. Xuan, W. Research on Opening Performance of Metal Diaphragm in Double Pulse Solid Rocket Motor. *J. Phys. Conf. Ser.* **2023**, *2478*, 072079.
20. Liu, H.; Zeng, J.; Yu, H.; Zhu, W. Research progress of isolation device and its materials for solid pulse motor. *J. Aerosp. Manuf. Technol.* **2018**, *2*, 1–5+10.
21. Li, S.; Yu, L.; Zhang, T.; Zhuo, C.; Gan, Y. Study on the open pressure of metal diaphragm in a compartment double-pulse solid rocket motor. *J. Ordnance Equip. Eng.* **2022**, *43*, 9–13.
22. Shi, R.; Wang, C.; Chang, Y. Design and experimental study of aluminum membrane diaphragm for dual-pulse solid rocket motor. *Solid Rocket. Technol.* **2013**, *36*, 190–194.
23. Xin, C.; Zhu, X.; Xue, Z.; Wang, J. *Handbook of Material Parameters for Finite Element Analysis*; China Machine Press: Beijing, China, 2022.
24. *ASTM B209-14*; Standard Specification for Aluminum and Aluminum-Alloy Sheet and Plate. ASTM International: West Conshohocken, PA, USA, 2014.
25. *GB/T 699-2015*; Carbon Structural Steels. Standards Press of China: Beijing, China, 2015.
26. Kong, H.Y. Study on the Mechanical Behavior of Multi-Layer Gradient Aluminum Honeycomb Panels under Impact and Large Deformation. Master's Thesis, Lanzhou University of Technology, Lanzhou, China, 2020. [CrossRef]
27. Zhang, D.; Mao, K.; Islam, M.S.; Andreasson, E.; Kao-Walter, S. *Powerful Modelling Techniques in ABAQUS to Simulate Failure of Laminated Composites*; Blekinge Tekniska Högskola: Karlskrona, Sweden, 2016. Available online: https://urn.kb.se/resolve?urn=urn:nbn:se:bth-11934 (accessed on 20 September 2024).
28. Li, Y.M. *Principles of Solid Rocket Motor*; Beihang University Press: Beijing, China, 2020.